Experimental Study of Supersonic Turbulent Flow on a Blunted Axisymmetric Body

D. S. Dolling* and W. K. Gray†
The University of Texas at Austin, Austin, Texas

Surface pressure distribution and turbulent boundary-layer velocity profiles have been measured on a tangent-ogive cylinder model at small angles of attack (0-4.5 deg) in a high Reynolds number, Mach 3 airflow. The model wall temperature was approximately adiabatic. The measurements were made using pointed, tangent-hemisphere, and flat-faced nose tips. The effects of tip blunting on the wind- and lee-side velocity profiles, integral thicknesses, shape factor, power law exponent, skin-friction coefficient, and wake strength parameter are presented. It is shown that the results obtained using different geometry tips can be correlated using bluntness length scale obtained by integration of the local tip surface angle from the stagnation point to the point corresponding to shock detachment.

Nomenclature

B = bluntness length scale [Eq. (1)]
C_f = skin-friction coefficient
D = cylinder diameter (Fig. 1)
D_{p_b} = additional drag due to tip blunting
H = shape factor ($=\delta^*/\theta$)
M = Mach number
n = exponent in velocity profile power law
P = pressure
Re = Reynolds number
S = distance along body surface measured from tip
u, U = velocity component in x direction
X = distance along body axis from pointed tip (Fig. 1)
y = distance normal to body surface
α = angle of attack
δ = boundary-layer thickness
δ^* = boundary-layer displacement thickness
θ = boundary-layer momentum thickness
Λ = wake strength parameter
ϕ = circumferential position (Fig. 1)

Subscripts

c = critical value
e = value at boundary-layer edge
t = pitot
w = value at the wall
0 = stagnation
∞ = undisturbed freestream

Introduction

ONE of the fundamental objectives of current computational fluid dynamics research is to predict the forces and moments on bodies in high-speed flows. An important class of flows is that over axisymmetric bodies such as projectiles. A review of present capabilities together with a bibliography of the recent experimental and numerical work, has been compiled by Sturek;[1] the reader is referred to it for details. In summary, it is clear that, although many parameters important to designers can now be calculated with acceptable accuracy (at least for simple geometries at small α), much remains to be done, particularly with respect to modeling the three-dimensional (3-D) turbulent boundary-layer development.

Accurate prediction of the three-dimensional boundary layer is essential for spin-stabilized bodies where the interaction of the surface spin with the cross flow produces asymmetries in the boundary layer. These asymmetries generate a side force (the Magnus force) whose net value is the sum of relatively small pressure and shearing forces (of different sign). Since both components originate in the viscous region, satisfactory predictions of the Magnus force require very accurate modeling of the boundary layer. To evaluate numerical simulation methods and to understand flow phenomena better, detailed experimental data are needed, both for spinning bodies and for the baseline case of zero spin.

The data base generated over the past decade includes overall aerodynamic coefficients obtained from firing tests and also detailed flowfield measurements made in wind tunnels. A large fraction of the wind tunnel studies has used tangent-ogive[2-6] and secant-ogive[7-11] cylinder models, with[5,8-11] and without conical boattails. Both spinning[2,4,7,9] and stationary models have been tested. Other than the tests of Refs. 10 and 11, which were made at $M_\infty = 0.97$ and 0.94, respectively, most of the work is in the supersonic regime ($2 \leqq M_\infty \leqq 4$). The published data are primarily mean flow measurements and include P_w, profiles of P_t and u/Ue vs y, and C_f. Other than Refs. 6, 10, and 11, in which tangent-hemisphere and flat nose tips were used, all the tips tested were pointed. Except in the work of Refs. 2-4, where the tip was pointed but its angle was large enough to cause shock detachment, the shocks were all attached.

In practice, projectile nose tips are generally blunt and the shock wave is detached. There is some evidence that this may increase the Magnus force.[12] Although the influence of tip bluntness on transition has been studied extensively (i.e., 31 references, including 4 review papers, are cited in the recent work of Stetson[13]), the effects on the subsequent turbulent boundary layer are less well documented. In the current study, surface pressures and boundary-layer velocity profiles have been measured on pointed and blunted tangent-ogive cylinder models in a high Reynolds number, Mach 3 airflow. The primary objective was to investigate the influences of tip blunting on the boundary-layer properties and generate detailed data for comparison with numerical work being carried out at the U. S. Army Ballistic Research Laboratory. A description of the experiment and the results are given in this paper. In a follow-up paper, the numerical method and comparisons with experiment will be presented.

Received March 1, 1985; revision received Oct. 21, 1985.

*Assistant Professor, Department of Aerospace Engineering and Engineering Mechanics. Senior Member AIAA.

†Lieutenant, U.S. Navy; formerly Graduate Student, Gas Dynamics Laboratory, Princeton University, Princeton, NJ.

Experimental Methods

Wind Tunnel

The experiments were carried out in the Princeton University 20×20 cm supersonic, high Reynolds number, blowdown tunnel. At the test station, the nominal value of M_∞ was 2.95. For all tests, the settling chamber conditions were $P_0 = 6.8 \times 10^5$ Nm^{-2} $\pm 1\%$ and $T_0 = 265$ K $\pm 5\%$, respectively, giving a nominal test section $Re_\infty = 6.3 \times 10^7$ m^{-1}. The model wall temperature was within 3% of the adiabatic value.

Models

A sketch of the model and coordinate system is shown in Fig. 1. Two models were built because there was insufficient internal space to instrument both the cylinder and the ogive-tip section on a single model. Model 1 had the ogive soldered to the cylinder and could be fitted with pointed, flat-faced, and tangent-hemisphere nose tips. The tip details and their designations are also given in Fig. 1. Only the cylinder was instrumented with pressure tappings and had seven streamwise rows of 20 tappings at the circumferential stations $\phi = 0$, 30, 60, 90, 120, 150, and 180 deg. The wall temperature was monitored using three chromel-alumel thermocouples installed in the cylinder.

Model 2 had separate cylindrical, ogive, and tip sections (P, R3, and F3 only), which could be fitted together using internal cylindrical guides and setscrews. The ogive and tips F3 and R3 were instrumented with two streamwise rows of tappings 180 deg apart. Because of internal space constraints, tip P was not instrumented. By aligning the tap rows on the ogive and the tip and then rotating the assembly relative to the cylinder, pressure distributions along opposing ϕ pairs (0-180 deg, 30-210 deg, etc.) were obtained.

Both models were secured in the tunnel using an axial sting downstream of the cylinder. A ball-joint adapter, restricting motion to the vertical plane only, permitted angle-of-attack settings in the range $-4.5 \text{ deg} \leqq \alpha \leqq 4.5$ deg.

Angle of Attack

The position $\alpha = 0$ deg was set iteratively. Several runs were made and α was adjusted until pressure distributions along the rows $\phi = 0$, 90, and 180 deg were within $\pm 1\%$ of each other. Inviscid calculations of P_w along $\phi = 0$ and 180 deg indicated that a $\pm 1\%$ variation corresponds to an accuracy in α of ± 0.2 deg. Other values of α were then set by displacing the tip a precomputed distance. The additional error in doing so is estimated to be ± 0.05 deg. Before a run, the cross wires of a telescopic sight were focused on the model tip. Vibration was observed on startup (and at shutdown), but during the test the model was steady at the same position as before startup.

Measurements and Data Documentation

The model configurations for which wall pressure distributions and pitot pressure surveys were obtained are listed in Tables 1 and 2, respectively. The data, in the form P_w(Nm^{-2}) and P_w/P_∞ vs X/D and P_t(Nm^{-2}) and u(m/s) vs y(m), are available in hard copy form or on a 9-track, 1600-bpi magnetic tape. (Copies of both can be obtained from the first author.)

The locations $X/D = 3.26$, 5.05, and 6.33 at which the pitot surveys were made are referred to as stations 1, 2, and 3, respectively, in the remainder of the text. Note that for the blunt tip models, X/D is measured relative to the virtual (pointed) origin (Fig. 1).

The pitot probe tip was made of flattened tubing and had a height of 0.18 mm (0.007 in.). Data taken less than 1½ probe heights above the wall were judged to be within the probe interference zone and were discarded. Velocity profiles were obtained from the pitot profiles assuming that: 1) $P(y) = P_w$ and 2) $T_0(y) = T_{0_\infty}\ [1 + 0.05(1 - y/\delta)]$. Assumption 1 was verified experimentally. Static pressure surveys at stations 1 and 2 using tip F3 showed that the maximum variation was $\pm 2\%$.

The velocity profiles were analyzed using a boundary-layer code developed originally by Sun and Childs.[15] It uses an iterative technique to fit the data to the combined law of the wall/law of the wake. The wall/wake parameters are varied until the deviation of the data from the combined law are minimized. In all cases, good fits were obtained. The values of δ, δ^*, θ, H, C_f, and Λ given below are from this code. The overall accuracy of δ^*, θ, C_f, and Λ is estimated to be better than $\pm 10\%$.

Discussion of Results

Wall Pressures

As indicated in Table 2, boundary-layer surveys were made along $\phi = 0$ and 180 deg for $\alpha = 0$ and 2.9 deg. The streamwise pressure distributions in which these profiles develop are shown in Fig. 2. Each data band includes results for the seven tips and has a variation of about $\pm 1.5\%$ about the mean value. No systematic effects of blunting are detectable within each band.

Pressure distributions on the ogive (for tips R3 and F3) at $\alpha = 0$ deg are shown in Fig. 3. For clarity, the data points near the tip are connected by straight lines. The exact positions of tips R3 and F3 are $X/D = 0.309$ and 0.404, respectively. The tap positions on the tips are shown in the inset

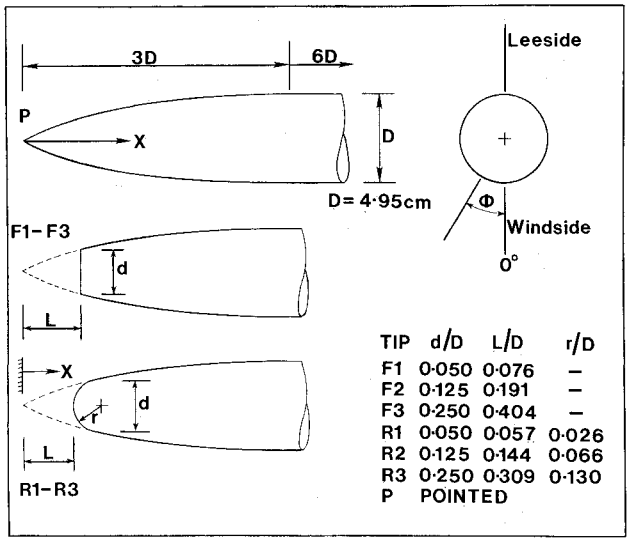

Fig. 1 Models and coordinate system.

Table 1 Configurations for which pressure distributions were measured

Configuration	Pressure distributions	α, deg	ϕ, deg
Model 1, all tips	Cylinder body	0,2.9	0-180 (30)
Model 2, tip P	Ogive	0,1,2 2.9 4.45	0,180 0-180 (30) 0,180
Model 2, tip R3	Ogive and tip	0,1,2 2.9 4.45	0,180 0-180 (30) 0,30,60,120,150,180
Model 2, tip F3	Ogive and tip	0 1.5,2.9 4.45	0,180 0-180 (30) 0,30,150,180

sketches. By $X/D=0.5$, the distributions for the two cases are essentially coincident. Thus, the influence of blunting is confined to the tip itself and to a very short region downstream of the junction with the ogive. Data for tip P (which could not be obtained further upstream than $X/D=1.5$) are also shown in Fig. 3. Agreement between the three data sets is good.

The pressures at taps 1′ and 1 on tips R3 and F3, respectively, are within 1% of P_{t_2}. For F3, $P_w=P_{t_2}$ over most of the face, but in the strong expansion around the tip corner P_w decreases below P_∞. The subsequent recovery to the ogive value occurs through a conical recompression shock wave (Fig. 4a). Here, "ogive value" refers to the pressure measured using tip P. In studies at $M_\infty=2.3$, the same geometry tip was tested, and similar shock patterns were reported.[1,12] No recompression shocks were observed with the R series tips. The shock pattern obtained for R3 (Fig. 4b) is typical of the three cases tested. The weak compression indicated by the arrow is caused by a very small step, 5 μm high, where the tip and ogive sections join.

Distributions for tips F3 and P at $\alpha=2.9$ deg are shown in Fig. 5. For clarity, data for R3 are not shown. Except on the tip itself, they agree well with the results for F3 and P. With F3, the wind-side recompression shock moves upstream and increases in strength, whereas the opposite occurs on the lee side. The shadow photograph confirms this (Fig 4c). For R3, a series of interior shocks occurs on the ogive wind side (Fig. 4d). These are very weak and have no measurable effect on P_w. Similar patterns were seen with tips F1 and R2. It has been suggested that these waves result from the reflection of expansion waves (downstream of the sonic point) from the bow shock and sonic line, which are then reflected from the body.[16] That this process would be highly geometry-dependent is a plausible explanation of its appearance and disappearance with small changes in tip shape.

Summarizing, P_w recovers rapidly to the ogive value, even with significant blunting. X_{ew}, the distance for completion of entropy wake effects on the pressure distribution, is small. For the cases tested here, $X_{ew}/D \leqq \sim 0.7$. In the absolute sense, the different growth rates of δ^* generated by different tips will cause small differences in P_w along the body. The differences are well within the normal range of experimental scatter and, consequently, are not detectable.

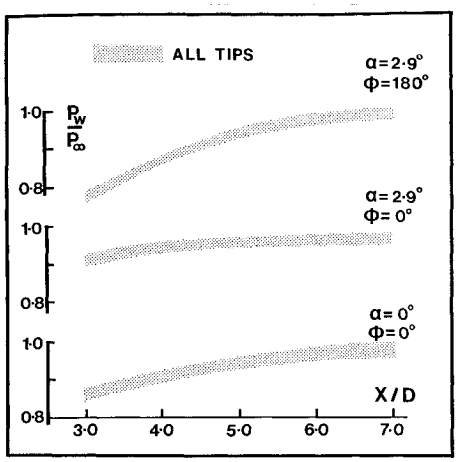

Fig. 2 Pressure distribution on cylinder body.

Table 2 Locations of boundary-layer surveys

Configuration	α, deg	ϕ, deg	X/D
Model 1, all tips	0,2.9	0,180	3.26,5.05,6.33

Table 3 Shape factor and wake strength parameter ($\alpha=0$ deg)

		H			Λ		
		Station			Station		
B, mm	Tip	1	2	3	1	2	3
—	P	5.26	5.21	5.08	0.55	0.77	0.57
1.34	R1	5.38	5.26	5.07	0.67	0.85	0.60
1.99	F1	5.39	5.22	5.08	0.57	0.78	0.71
3.33	R2	5.16	5.13	5.09	0.66	0.82	0.76
4.99	F2	5.11	5.11	5.06	0.79	0.98	0.89
6.58	R3	4.51	4.72	4.80	0.61	0.92	0.88
9.97	F3	4.05	4.16	4.43	0.51	0.82	0.98

Boundary-Layer Properties

$\alpha=0$ Deg

It is well known that tip bluntness and α influence the transition location.[17] In this study, the transition location was deduced from shadow photographs and is therefore only qualitative and indicative of general trends. For tip P, $(S/D)_{tr} \sim 0.9-1.5$. With the R series tips, the higher entropy, lower Mach number fluid adjacent to the surface delays transition. In contrast, transition for the F series tips occurs earlier than with tip P and is in the range $\sim 0.7 \leqq$

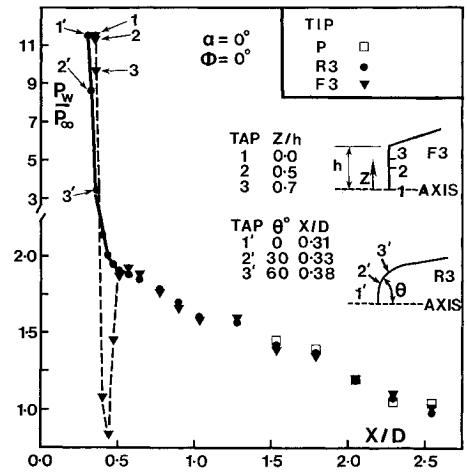

Fig. 3 Pressure distribution on the ogive and tip ($\alpha=0$ deg).

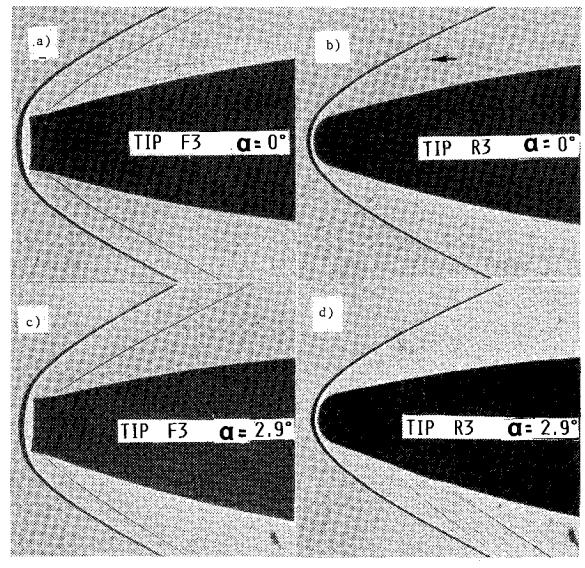

Fig. 4 Shadow photographs using tips R3 and F3.

$(S/D)_{tr} \leqq \sim 1.1$. The reason why is not entirely clear, but it is possible that the recompression shock wave acts as a "trip" that overcomes the delaying influence of the higher entropy, lower Mach number fluid generated by the bow shock.

Velocity profiles are shown in Fig. 6. For clarity, only four profiles are shown at each station. y and u are normalized by D and U_∞, respectively, rather than δ and U_e, in order to highlight the effects on the profile shape and thickness. At all stations, blunting retards the profile and increases its thickness. The latter is caused mainly by the progressively larger entropy wake associated with increased blunting and not from growth of the boundary layer proper. Although y_e is difficult to define precisely for tips R3 and F3, the region in which the boundary-layer profile turns upward and merges with the entropy wake is discernible.

Values of n obtained from least-squares curve fits to the power law approximation $u/U_e = (y/\delta)^{1/n}$ are shown vs Re_θ in Fig. 7a. The shaded band brackets data for about 80 profiles from four different zero-pressure-gradient studies.[18] The expansion over the ogive generates fairly full profiles at station 1 ($n = 5.9$-6.9). Over the upstream section of the cylinder dP/dx is positive which reduces n to the range 5.6-6.0, then as $dP/dx \to 0$ with increasing X/D, n increases. The distance required for n to recover to values within the shaded band is a strong function of tip bluntness. For P and R1, the recovery is complete by station 3. For R3, linear extrapolation indicates recovery at $X/D \approx 20$-30, whereas for F3 the recovery has not even begun by station 3.

The influence of different tips on n (and on other profile and integral parameters) can be correlated when plotted in terms of a bluntness length B, given by

$$B = \int_0^{\theta_d} \delta_s \, dS \quad \text{(see inset, Fig. 7b)} \qquad (1)$$

At $\alpha = 0$ deg, the values of B(mm) are given in Table 3. In terms of increasing B, the different geometry tips occur in alternate order. Figure 7b shows n as a function of B/D. By station 3 there is a consistent trend of decreasing n with increasing B/D. Viewed simply, this reflects the "shorter history" caused by the Reynolds number reduction that occurs with increased blunting.

The additional pressure drag, Dp_b, due to tip bluntness, can also be used as a correlating parameter. Both Dp_b and B give similar data correlations.[6] The utility of B is that it can be calculated easily, given the tip geometry and M_∞.

The development of $\delta^*$and Θ is shown in Fig. 8. For clarity in this and subsequent figures, the data points are joined by straight lines. Values of H and Λ are given in Table 3. At any station, H is approximately constant up to a critical value of blunting B_c and then decreases. B_c increases with X/D, reflecting the progressive dissipation of entropy wake effects. At station 3, only the bluntest tips (R3 and F3) influence H.

Although H is approximately constant for $B < B_c$, δ^* and Θ are influenced significantly by small amounts of blunting. Their detailed behavior with B is complex and depends on X/D. However, with increasing X/D, a consistent trend emerges. As shown in Figs. 9a and 9b, by station 3 ($X/D = 6.33$), both δ^* and Θ increase with increasing B/D.

C_f as a function of X/D is shown in Fig. 10a. At any station, blunting initially decreases C_f but, beyond a certain value, increases it. At the upstream stations, only tips R3 and F3 generate values greater than the value for tip P. The results at station 3 are qualitatively similar, but the increase after the initial decrease is much smaller so that C_f for all blunt tips is below, but within, 10% of the value for P. Further, other than R3 at station 1 and F3 at stations 1 and 2, the data correlate reasonably well with Re_θ (Fig. 10b). The weak adverse pressure gradient causes C_f to fall below the zero-pressure-gradient Van Driest II prediction[19] shown by the solid line, but the discrepancy is typically less than 10%.

Λ is strongly influenced by tip blunting (Table 3). In all cases, the adverse pressure gradient causes an increase from stations 1 to 2. Except for F3, Λ then decreases as the pressure gradient relaxes. Small amounts of blunting have a significant effect on Λ, even six calibers from the tip. At this station, only tips P and R1 have values of Λ within the ac-

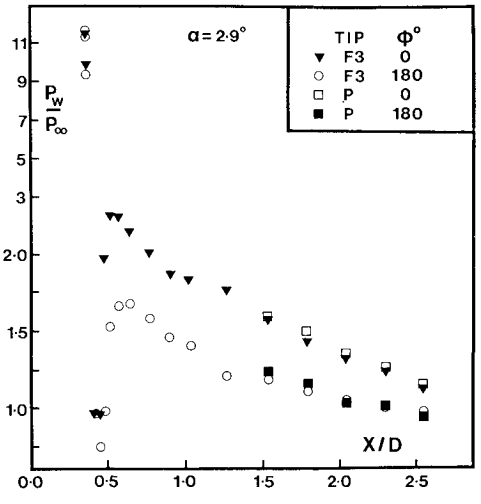

Fig. 5 Pressure distributions on the ogive and tip ($\alpha = 2.9$ deg).

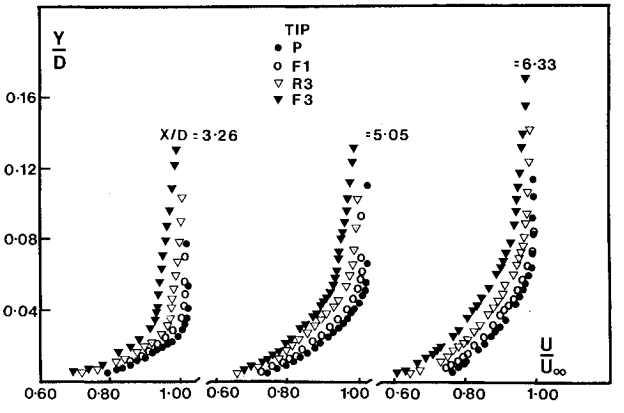

Fig. 6 Boundary-layer velocity profile development ($\alpha = 0$ deg).

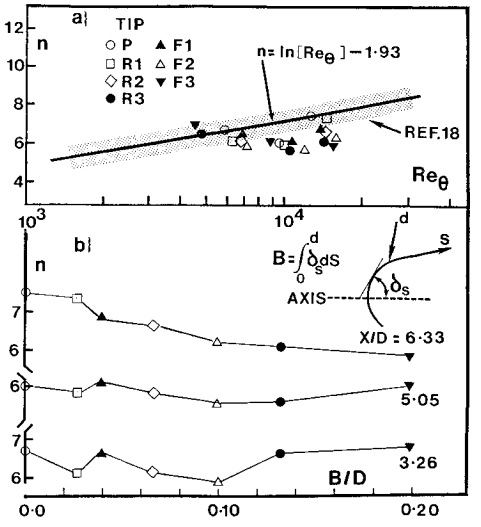

Fig. 7 Boundary-layer power law exponent n as a function of Re_θ and B/D.

cepted range for zero-pressure-gradient turbulent boundary layers. With increased blunting, Λ increases and, as shown in Fig. 9c, correlates reasonably well with B/D.

In summary, the effects of tip bluntness on the inner part of the profile (as reflected in C_f) dissipate in a fairly short streamwise distance from the tip. The effects on the outer region, which are much more directly affected by the entropy wake, require significantly larger distances.

$\alpha = 2.9$ Deg

δ^* and Θ along $\phi = 0$ and 180 deg are plotted in Figs. 11 and 12, respectively. On the lee side, the combination of the stronger adverse dP/dx and the cross flow increases the magnitudes and growth rates of both quantities by a factor of 2 or more over their values at $\alpha = 0$ deg. On the wind side, both the absolute values and growth rates are lower. On the lee side the effects of blunting are the same at all stations, whereas on the wind side the effects depend on position. H vs B/D is shown in Fig. 13. The effects of blunting are greater on the lee side. The wind-side trends are the same as at $\alpha = 0$ deg, except that the weaker dP/dx results in a more rapid dissipation of entropy wake effects. At station 1, only the bluntest tips (R3 and F3) influence H. By station 3, H for all seven tips is within 2% of the mean value, and the trend of decreasing H for $B > B_c$ is barely detectable. The opposite is true on the lee side. At station 1, even tips R1 and F1 noticeably influence H. B_c does increase with X/D but less rapidly than on the wind side or at $\alpha = 0$ deg.

Figure 14a shows n vs Re_θ. The zero-pressure-gradient data band is again shown for comparison. On the wind side, the weak adverse dP/dx and favorable $dP/d\phi$ induce cross flow away from $\phi = 0$ deg, generating full profiles. Since $d\Theta/dx$ is small (Fig. 12), this causes large values of n at low values of Re_θ. In contrast, on the lee side, the stronger adverse dP/dx between stations 1 and 2 retards the profiles. This decreases n but increases Θ and $d\theta/dx$. Thus, by station 2, all profiles have low values of n but high values of Re_θ. As dP/dx relaxes, the expected trend of increasing n with increasing Re_θ is seen in all cases.

C_f on the wind and lee sides is shown in Figs. 14b and 14c, respectively. At a given station and with a given tip, the stronger adverse dP/dx along $\phi = 180$ deg results in lower values of C_f than along $\phi = 0$ deg. For all tips, C_f decreases with X/D, more rapidly on the lee side than wind side. Downstream of station 1, which is affected by expansion over the ogive, the data correlate reasonably well with Re_θ. On the wind side, where dP/dx is only mildly adverse, the agreement with the zero-pressure-gradient Van Driest II prediction is good. On the lee side, the stronger adverse dP/dx results in values about 20% below the prediction.

In general, at a given station, C_f increases with increased blunting. On the wind side, the influence of blunting dissipates rapidly. At station 1, C_f for tips P, R1, F1, R2, and F2 is within 4% of the mean value. Tips R3 and F3 are 11% and 21%, respectively, above the mean. By station 2,

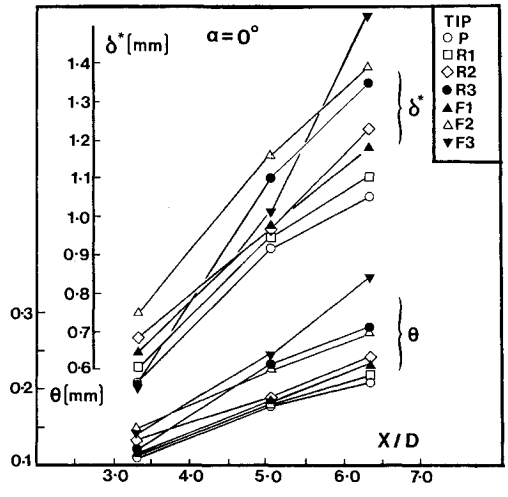

Fig. 8 Streamwise development of δ^* and θ ($\alpha = 0$ deg).

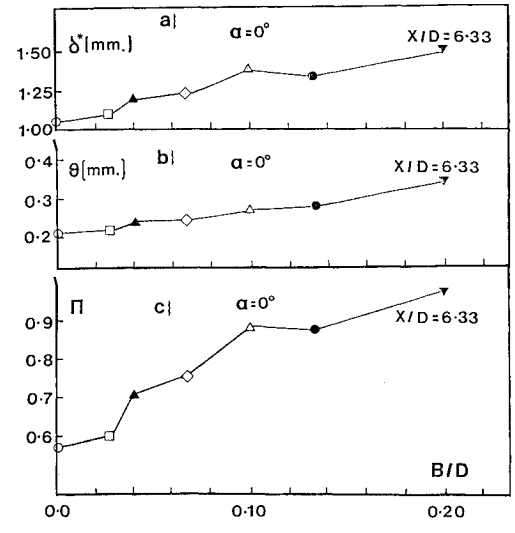

Fig. 9 Correlation of δ^*, Θ, and Λ with B/D at station 3 ($\alpha = 0$ deg).

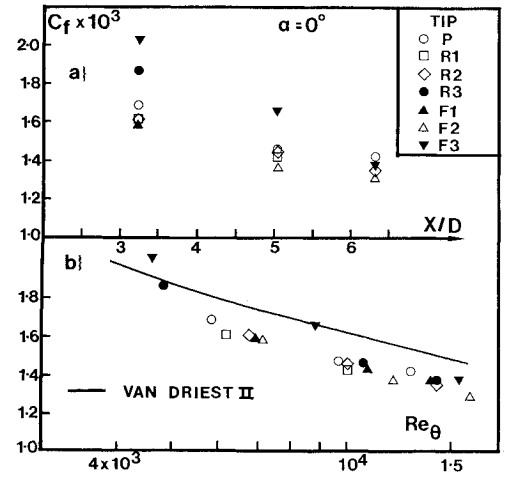

Fig. 10 Skin-friction coefficient as a function of X/D and Re_θ.

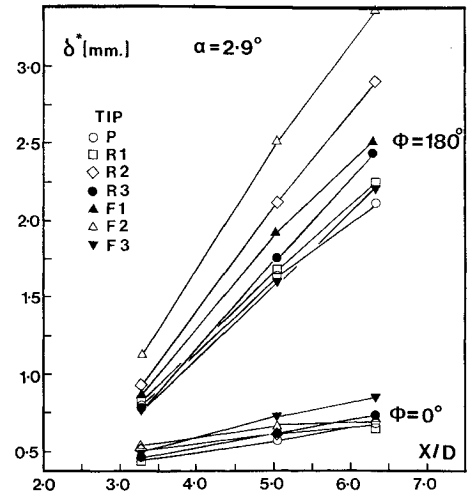

Fig. 11 Wind- and lee-side development of δ^* ($\alpha = 2.9$ deg).

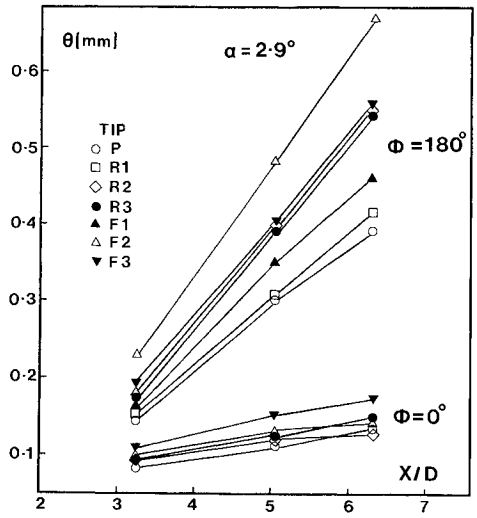

Fig. 12 Wind- and lee-side development of Θ ($\alpha = 2.9$ deg).

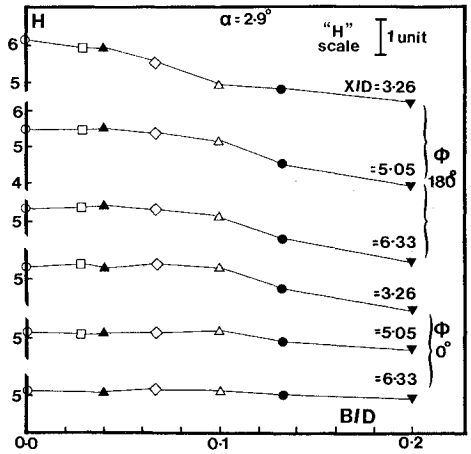

Fig. 13 Boundary-layer shape factor as a function of B/D ($\alpha = 2.9$ deg).

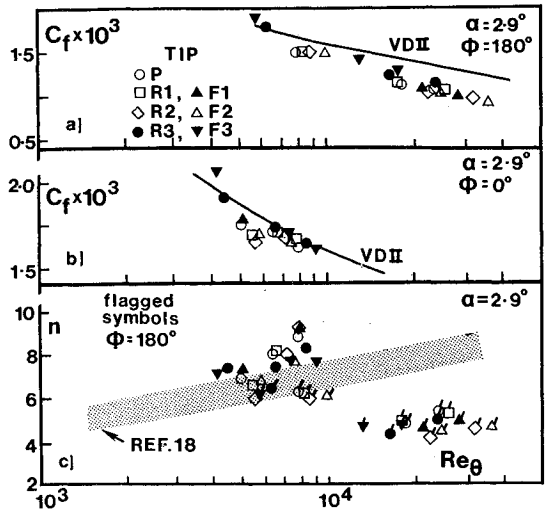

Fig. 14 Velocity profile power law exponent and skin friction coefficient as a function of Re_θ ($\alpha = 2.9$ deg).

C_f for all tips is within 3% of the mean value and no systematic influence of B is detectable. In contrast, on the lee side, the range of C_f at a given station increases with X/D. At station 1, C_f for P, R1, F1, R2, and F2 are all within 1% of the mean value, with R3 and F3 20% and 28%, respectively, above the mean. However, at station 3, C_f decreases from .00107 to .00092 as B/D increases from 0 to 0.1, then increases to .00131 as B/D increases to its maximum.

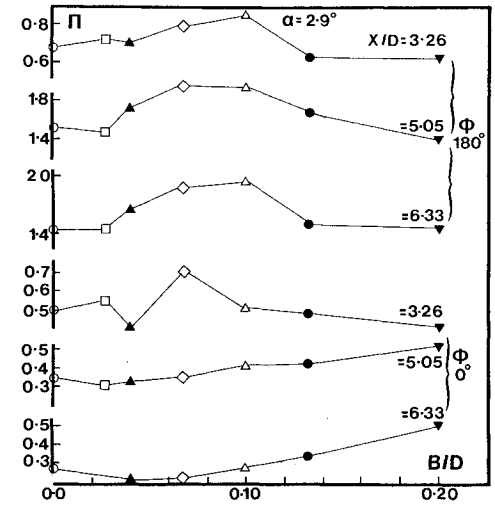

Fig. 15 Wake strength parameter as a function of B/D ($\alpha = 2.9$ deg).

Λ vs B/D is shown in Fig. 15. For a given tip (except F3), the wind-side values of Λ decrease with X/D. At station 3 (where $dP/dx \approx 0$), Λ is in the range 0.22-0.34, substantially below the $\alpha = 0$ deg case (Table 3). On the lee side, Λ increases by a factor of 2 of more from station 1 to 2 but between stations 2 and 3 typically changes less than 5%. The trend with B is consistent from station to station; intermediate values of B increase Λ, but a large amount of blunting decreases it to the pointed value.

Overall, the effects of small α on the wind- and lee-side boundary layers are qualitatively similar for all tips. However, as B increases, the detailed behavior of a given parameter at a fixed station is generally complex, particularly at the upstream stations where the combined influences of the different starting conditions, transition location, and external entropy wake interact strongly.

Concluding Remarks

An experimental study has been made of the effects of nose tip blunting on the surface pressure distribution and the wind- and lee-side boundary-layer development on a tangent-ogive cylinder model. The tests were made at small angles of attack (0-4.5 deg) in a high Reynolds number, Mach 3 airflow under approximately adiabatic wall temperature conditions. Models with pointed, tangent-hemisphere, and flat-faced nose tips were tested. The results show that:

1) The distance for completion of entropy wake effects on the surface pressure distributions is small. Even with significant tip blunting, the effects are confined to the tip itself and a short region downstream of the junction with the ogive.

2) The bow shock generated by a blunt tip not only creates an entropy wake but also affects both the initial conditions for boundary-layer growth and transition. Hence, tip bluntness has a strong influence on the development of all boundary-layer properties. Since each of these properties has a different sensitivity to tip blunting, the streamwise station at which the effects of blunting can be considered complete is a function of the particular property selected.

3) The effects of different tip shapes can be correlated in terms of a bluntness length B. B is obtained by integrating the local tip surface angle from the stagnation point to the point corresponding to shock wave detachment. At stations close to the ogive shoulder, the interaction of the three factors given above generally results in a complex relationship between any property and B. Further downstream, simpler trends with B are observed and good correlations can be obtained.

4) The effects of angle of attack are qualitatively similar for all tips. In general, entropy wake effects dissipate more rapidly in the near-zero pressure gradient on the wind side than on the lee side, which has a stronger adverse pressure gradient. The effects of different tip shapes can also be correlated as a function of B.

Acknowledgments

This work was supported by the Army Research Office under grants DAAG 29-84-M-0432 and DAAG 29-77-G-0234, monitored by Dr. R. Singleton. The experimental phase of the study was carried out at the Gas Dynamics Laboratory of Princeton University. Many helpful discussions with Professors S. M. Bogdonoff and G. S. Settles are gratefully acknowledged.

References

[1]Sturek, W. B., "Application of CFD to the Aerodynamics of Spinning Shell," AIAA Paper 84-0323, Jan. 1984.

[2]Sturek, W. B., "Preliminary Surveys of the Three Dimensional Boundary Layer on a Yawed Spinning Body of Revolution," U. S. Army Ballistic Research Laboratory BRL-MR-2501, July 1975.

[3]Sturek, W. B. and Reba, J. J., "Measurements of Wall Static Pressure on a Yawed Tangent Ogive Cylinder Model," U. S. Army Ballistic Research Laboratory BRL-MR-2699, Nov. 1976.

[4]Sturek, W. B. and Danberg, J. E., "Experimental Measurements of the Turbulent Boundary Layer on a Yawed, Spinning Slender Body," U. S. Army Ballistic Research Laboratory BRL-R-1954, Jan. 1977.

[5]Reklis, R. P. and Sturek, W. B., "Surface Pressure Measurements on Slender Bodies at Angle of Attack in Supersonic Flow," U. S. Army Ballistic Research Laboratory ARBRL-MR-02876, Nov. 1978.

[6]Gray, W. K., "An Experimental Investigation of Tip Bluntness Effects on the Turbulent Compressible Boundary Layer on an Axisymmetric Body," Thesis 1495-T, Mechanical and Aerospace Engineering Department, Princeton University, Princeton, NJ, March 1981.

[7]Kayser, L. D. and Sturek, W. B., "Experimental Measurements in the Turbulent Boundary Layer of a Yawed, Spinning Ogive-Cylinder Body of Revolution at Mach 3. Part I. Description of the Experiment and Data Analysis," U. S. Army Ballistic Research Laboratory ARBRL-MR-02808, Jan. 1978.

[8]Kayser, L. D., Yanta, W. J., and Sturek, W. B., "Measurements in the Turbulent Boundary Layer of a Yawed, Spinning Body of Revolution at Mach 3.0 with a Laser Velocimeter and Impact Probe," U. S. Army Ballistic Research Laboratory Tech. Rept. ARBRL-TR-02074, May 1978.

[9]Kayser, L. D. and Sturek, W. B., "Turbulent Boundary Layer Measurements on the Boattail Section of a Yawed, Spinning Projectile Shape at Mach 3.0," U. S. Army Ballistic Research Laboratory ARBRL-MR-02880, Nov. 1978.

[10]Nietubicz, C. J., Inger, G. R., and Danberg, J. E., "A Theoretical and Experimental Investigation of a Transonic Projectile Flow Field," AIAA Paper 82-0101, Jan. 1982.

[11]Reklis, R. P., Danberg, J. E., and Inger, G. R., "Boundary Layer Flows on Transonic Projectiles," AIAA Paper 79-1551, June 1979.

[12]Sturek, W. B., Guidos, B., and Nietubicz, C. J., "Navier-Stokes Computational Study of the Magnus Effect on Shell with Small Bluntness at Supersonic Speeds," AIAA Paper 82-1341, Aug. 1982.

[13]Stetson, F., "Nose Tip Bluntness Effects on Cone Frustrum Boundary Layer Transition in Hypersonic Flow," AIAA Paper 83-1763, July 1983.

[14]Dolling, D. S. and Gray, W. K., "Compilation of Wall Pressure and Turbulent Boundary Layer Data for Supersonic High Reynolds Number Flow over a Blunted Tangent Ogive Cylinder at Small Angles of Attack," Gas Dynamics Laboratory, Princeton University, Princeton, NJ, Rept. 1585-MAE, Sept. 1982.

[15]Sun, C. C. and Childs, M. E., "A Modified Wall-Wake Velocity Profile for Turbulent Compressible Boundary Layers," *Journal of Aircraft*, Vol. 10, June 1973, pp. 381-383.

[16]Perkins, E. W., Jorgensen, L. H., and Sommer, S. C., "Investigation of the Drag of Various Axially Symmetric Nose Shapes of Fineness Ratio 3 for Mach Numbers from 1.24 to 7.4," NACA Rept. 1386, 1958.

[17]Ericsson, L. E., "Correlation of Attitude Effects on Slender Vehicle Transition," *AIAA Journal*, Vol. 12, April 1974, pp. 523-529.

[18]Settles, G. S. and Bogdonoff, S. M., "Separation of a Supersonic Turbulent Boundary Layer at Moderate to High Reynolds Numbers," AIAA Paper 73-666, July 1973.

[19]Hopkins, E. J., "Charts for Predicting Turbulent Skin Friction from the Van Driest Method (II)," NASA TN-D-6945, Oct. 1972.